Plasma density transition-based electron injection in laser wake field acceleration driven by a flying focus laser

Pan-Fei Geng(耿盼飞)[1,2], Min Chen(陈民)[1,2,†], Xiang-Yan An(安相炎)[1,2], Wei-Yuan Liu(刘维媛)[1,2], Xin-Zhe Zhu(祝昕哲)[1,2], Jian-Long Li(李建龙)[1,2], Bo-Yuan Li(李博原)[1,2], and Zheng-Ming Sheng(盛政明)[1,2]

[1] *Key Laboratory for Laser Plasmas (Ministry of Education), School of Physics and Astronomy, Shanghai Jiao Tong University, Shanghai* 200240, *China*
[2] *Collaborative Innovation Center of IFSA (CICIFSA), Shanghai Jiao Tong University, Shanghai* 200240, *China*

(Received 16 November 2022; revised manuscript received 16 December 2022; accepted manuscript online 27 December 2022)

By using a high-intensity flying focus laser, the dephasingless [*Phys. Rev. Lett.* **124** 134802 (2020)] or phase-locked [*Nat. Photon.* **14** 475 (2020)] laser wakefield acceleration (LWFA) can be realized, which may overcome issues of laser diffraction, pump depletion, and electron dephasing which are always suffered in usual LWFA. The scheme thus has the potentiality to accelerate electrons to TeV energy in a single acceleration stage. However, the controlled electron injection has not been self-consistently included in such schemes. Only external injection was suggested in previous theoretical studies, which requires other accelerators and is relatively difficulty to operate. Here, we numerically study the actively controlled density transition injection in phase-locked LWFA to get appropriate density profiles for amount of electron injection. The study shows that compared with LWFA driven by lasers with fixed focus, a larger plasma density gradient is necessary. Electrons experience both transverse and longitudinal loss during acceleration due to the superluminal group velocity of the driver and the variation of the wakefield structure. Furthermore, the periodic deformation and fracture of the flying focus laser in the high-density plasma plateau make the final injected charge also depend on the beginning position of the density downramp. Our studies show a possible way for amount of electron injection in LWFA driven by flying focus lasers.

Keywords: density transition injection, laser wakefield acceleration, flying focus laser

PACS: 41.75.Jv, 52.38.Kd, 52.65.Rr **DOI:** 10.1088/1674-1056/acae79

1. Introduction

Laser wakefield acceleration (LWFA) has attracted wide interest for its ultra-high acceleration gradient ($\sim$ GV/cm), which has applications in compact accelerators and radiation sources.[1–5] With the development of ultra-short ultra-intense laser and plasma physics, energy records of electrons from LWFA are constantly broken.[6–9] So far, maximum electron energy gain observed in LWFA has reached 7.8 GeV, which was realized in only 20 cm.[9] However, this is far from TeV energy required by future high energy colliders.[10,11] That is because the electron energy gain in traditional LWFA is mainly limited by three factors: laser diffraction, pump depletion and electron dephasing.[2–4] With the propagation of the laser, diffraction and pump depletion will reduce the laser intensity, and eventually it will no longer stably excite a strong wakefield. Dephasing is caused by subluminal group velocity of laser in plasmas. As electrons are accelerated to the relativistic energy, they will slip from the acceleration phase of wakefield to the deceleration phase, thus terminating the acceleration. Many efforts have been made to address these restrictions.[7–9,12–16] For example, the discharge capillary waveguide is usually used to guide the laser to solve the problem of laser diffraction. Multistage acceleration is expected to solve pump depletion. These studies rely on the successful control of the plasma condition, which is usually not easy to do.

Over recent years, with the improvement of the ability to manipulate the laser pulse in time and space,[17,18] several novel lasers have been proposed and used to excite wakefield.[19–22] In particular, in 2020, Caizergues *et al.*[21] and Palastro *et al.*[22] proposed a so-called dephasingless or phase-locked LWFA scheme, which has aroused great interest. Essentially, combining the axiparabola[23] and a radial dependent pulse front delay, they constructed a high-intensity flying focus laser to drive wakefield. Such axiparabola based flying focus lasers can possess simultaneously a long focal depth (tens of millimeters), a small focal spot (several microns) and a controllable group velocity.[24] Therefore, this dephasingless or phase-locked LWFA scheme not only overcomes dephasing, but also addresses the issue of laser diffraction. Furthermore, since the focal spot at different longitudinal positions can be continuously supplemented by light rays from radial positions, pump depletion is also partially solved. The energy scaling law of dephasingless or phase-locked LWFA implies that electron beams with TeV-level energy can be obtained in only a few meters.[21,22] Using an externally injected electron bunch with 200 MeV, Caizergues *et al.* have confirmed numerically the feasibility of phase-locked LWFA via particle-in-cell (PIC) simulations. However, this scheme is not

†Corresponding author. E-mail: minchen@sjtu.edu.cn
© 2023 Chinese Physical Society and IOP Publishing Ltd

self-consistently combined with the controlled injection process, such as density transition injection[25–28] or ionization injection,[29–31] which is widely used in normal LWFA. Due to a larger laser group velocity, the injection of electrons in phase-locked LWFA may be relatively difficult, which has not been studied, but is crucial for future experiments.

In this paper, we numerically study the density transition injection scheme in wakefield driven by an axiparabola based flying focus laser by using PIC simulations. The density transition can be generated by shocks.[32] We find that such injection is more difficult in phase-locked LWFA than usual LWFA. Specifically, a larger density gradient is required to eventually inject and accelerate a considerable amount of electrons. When the density gradient is relatively small, although some electrons can be injected into the bubble when the laser passes the density downramp, these electrons are soon thrown out of the bubble in subsequent oscillations, resulting in very few electrons remaining in the bubble and being accelerated. This is because of the oscillated laser group velocity. In order to inject amount of electrons, it is necessary to initially inject more electrons in the bubble and stay away from the tail of the bubble. It requires a larger density gradient, *i.e.*, increasing the density in high-density plateau or shortening the length of density downramp. Similar to density transition injection in traditional LWFA, a larger density gradient in phase-locked LWFA can inject and accelerate more electrons, but it reduces the energy gain of electrons. Furthermore, as high-intensity flying focus lasers experience periodic deformation and fracture during propagating in high-density plasmas, with the increase of the length of high-density plateau, electrons will be injected periodically. A longer high-density plateau leads to an unstable laser propagation, which also deteriorates the final energy spectrum of electrons. In the following, we numerically study the effects of the different parameters of the density profile on the electron injection.

2. Setting of simulation parameters

In order to study density transition injection of electrons in phase-locked LWFA, a parametric scan was carried out via a modified FBPIC (Fourier–Bessel particle-in-cell) code, which is a quasi three-dimensional (3D) program running in a cylindrical coordinate system,[33] where the flying focus laser module has been added.[34] The longitudinal profile of the plasma density used in simulations is composed of four parts, as shown in Fig. 1. The upramp allows the laser to enter the plasma smoothly, which is fixed as $L_{\rm up} = 100$ μm. A low-density plateau is mainly used to accelerate electrons, which is also fixed as $n_0 = 5 \times 10^{18}$ cm^{-3}. The density in high-density plateau n_1 and the length of downramp $L_{\rm down}$ determine the density gradient. The length of high-density plateau $L_{\rm flat}$ affects the laser propagation. Therefore, the parameters n_1, $L_{\rm down}$, and $L_{\rm flat}$ are variable in our simulations. Three sets of simulations have been performed to study the influence of plasma target parameters on density transition injection in phase-locked LWFA. The details of the parameters can be found in Section 3.

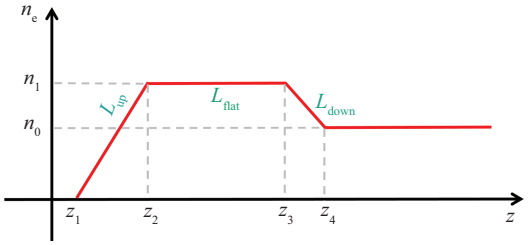


Fig. 1. Longitudinal profile of plasma density used in the simulation. The plasma starts at $z_1 = 600.06$ mm and consists of four parts: a linear density upramp with length $L_{\rm up}$, a high-density plateau with length $L_{\rm flat}$ and density n_1, a linear density downramp with length $L_{\rm down}$ and a low-density plateau with density n_0. For all simulations, parameters [$L_{\rm up}$, n_0] are fixed as [$L_{\rm up} = 100$ μm, $n_0 = 5 \times 10^{18}$ cm^{-3}], and parameters [$L_{\rm flat}$, $L_{\rm down}$, n_1] are varied.

An intense flying focus laser can be realized by combining an axiparabola and a radial dependent pulse front delay, as illustrated in Fig. 2(a). The axiparabola mirror is a reflective optical element, which focuses the rings with different radii in the incident beam at different longitudinal positions.[23,24] The typical shape of an axiparabola can be given by[23]

$$z_{\rm m}(r) = \frac{r^2}{4f_0} - \frac{Lr^4}{8f_0^2R^2} + \frac{L(R^2+8f_0L)r^6}{96f_0^4R^4}, \tag{1}$$

where f_0, R, and $|L|$ represent the focal length of a near-center ray, the radius of incident beam, and the length of focal line, respectively. As we can see from Eq. (1), in terms of geometry, the axiparabola mirror is a higher-order modification of the parabolic mirror, and the difference between the two is very small (only a few microns), which increases the difficulty of making mirrors experimentally. Nevertheless, such an axiparabola mirror has been successfully manufactured and used to generate a plasma waveguide that can guide an intense laser over 10 mm.[23,35] It is worth noting that the focal line of the axiparabola can be positive ($L > 0$) or negative ($L < 0$). The negative focal line means that the light with a larger radius in the incident beam is first reflected and focused at a smaller longitudinal position (see Fig. 2(a)). The parameters of axiparabola are selected as $f_0 = 608$ mm, $R = 30$ mm, and $L = -8$ mm. Here, a negative focal line is used, which is beneficial to the stable propagation of high-intensity flying focus laser in plasmas.[34] The real geometry of the axiparabola mirror calculated according to Eq. (1) is shown by the blue curve in Fig. 2(b). A radial-dependent pulse front delay is used to adjust the time when light rays with different radii reach the axiparabola mirror and are reflected, so as to control the group velocity of laser.[21,22,24,36] Meanwhile, such a delay also alleviates the unstable propagation of laser in plasmas.[34] In actual experiments, this delay can be introduced by a reflective

echelon[22] or chromatic optics[37] or the spatial light modulator and deformable mirror.[38]

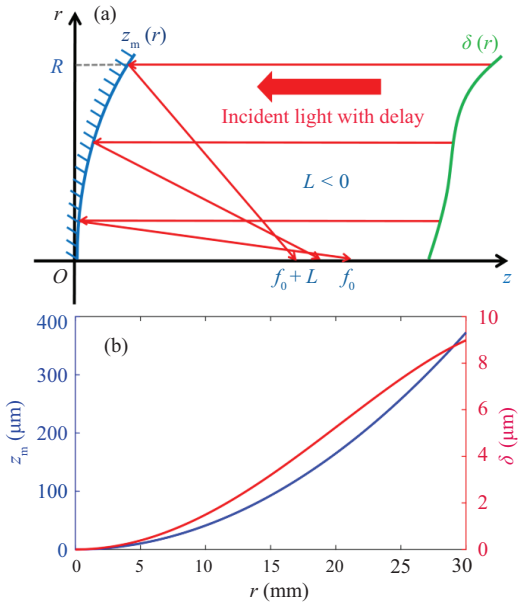


Fig. 2. (a) The schematic diagram of flying focus lasers realized by combining the axiparabola mirror z_m and a radial-dependent pulse front delay δ. An axiparabola with a negative focal line ($L<0$) focuses the light with a smaller radius in the incident beam at a larger longitudinal position. A radial-dependent pulse front delay can be used to adjust the time when the light reaches the mirror and is reflected, thus controlling the speed of the focal spot. (b) The real geometry of the axiparabola (the blue curve) given by Eq. (1) and delay function (the red curve) calculated according to Eq. (2) with $v_f = 1.00175c$, which ensures that the laser group velocity in low-density plateau is equal to c.

The relationship between group velocity v_f and delay function $\delta(r)$ can be expressed by[22]

$$\frac{\partial\delta(r)}{\partial r} = \left(\frac{c}{v_f} - \frac{1-z_m'^2}{1+z_m'^2}\right)\frac{2Lr}{R^2}, \tag{2}$$

where $z_m' = \mathrm{d}z_m/\mathrm{d}r$ is the derivative of mirror function to radial coordinate. In order to achieve phase-locked LWFA, the group velocity of the flying focus lasers in vacuum v_f needs to compensate the decrease of the laser group velocity in plasmas, *i.e.*, $v_f/c = 1 + n_e/2n_c$, with n_e being electron density and n_c being critical density for drive laser. Note that considering the numerical dispersion and the paraxial approximation made in calculating the theoretical group velocity, v_f needs to be further pre-compensated in our simulations, *i.e.*, $v_f/c = 1 + n_e/2n_c + \Delta_{num} = 1.00175$. The delay function $\delta(r)$ required to maintain the light speed c in low-density plateau is shown by the red line in Fig. 2(b), according to Eq. (2). The electric field expression of flying focus lasers is calculated by the time-dependent scalar diffraction theory.[36,39,40] The laser with a wavelength of $\lambda = 800$ nm is linearly polarized along the x direction. The normalized potential of laser pulse is $a_0 = eE/(m_e\omega c) = 1.5$, and the full width at half maximum (FWHM) duration is selected as $\tau = 15$ fs. The center of laser pulse is initially located at $z_0 = 600$ mm. The spatial resolution of simulations in the radial and longitudinal directions is selected as $\mathrm{d}r = \lambda/4$, $\mathrm{d}z = \lambda/8$, respectively. The transverse size of the simulation box is 300 μm.

3. Simulation results and analyses

In order to study the influence of plasma target parameters (n_1, L_{down}, L_{flat}) on injection in detail, three sets of comparative simulations have been performed: $\{L_{flat} = 100\ \mu\mathrm{m}, L_{down} = 10\ \mu\mathrm{m}, n_1 = [2n_0, 3n_0, 5n_0]\}$, $\{L_{flat} = 100\ \mu\mathrm{m}, n_1 = 5n_0, L_{down} = [10\ \mu\mathrm{m}, 20\ \mu\mathrm{m}, 30\ \mu\mathrm{m}]\}$, $\{L_{down} = 10\ \mu\mathrm{m}, n_1 = 5n_0, L_{flat} = [100\ \mu\mathrm{m}, 300\ \mu\mathrm{m}, 500\ \mu\mathrm{m}]\}$. For all cases, the charge of injected electrons at any moment is defined as the total charge of electrons with longitudinal momentum of $p_z > 200m_ec$ near the axis ($x \in [-3,3]$ μm, $y \in [-3,3]$ μm).

3.1. Effect of high plateau density on injection

In order to study the effect of the high plateau density n_1 on electron injection, we have performed a set of simulations with parameters $L_{flat} = 100$ μm, $L_{down} = 10$ μm, and $n_1 = [2,3,5]n_0$. The simulation results are shown in Figs. 3 and 4. Figure 3 shows spatial distribution of electron density at different instants. The first (Figs. 3(a), 3(f), 3(k)) and second (Figs. 3(b), 3(g), 3(l)) columns correspond to the moments before and after the laser enters the density downramp, respectively. The last column corresponds to the moment when the laser propagates about 3 mm. The red, green, and blue lines in Fig. 4(a) show variations of phase velocity of plasma wave v_{wp} along the density downramp, according to

$$v_{wp} = v_{fp} - \frac{\mathrm{d}\lambda_p}{\mathrm{d}t}, \tag{3}$$

where v_{fp} is the group velocity of flying focus lasers in plasmas. The second term on the right-hand side represents the expansion velocity of plasma wave in the density downramp, which is shown by the magenta lines in Fig. 4(a). Here, $\lambda_p(t) = 2\pi c\sqrt{m_e\varepsilon_0/n_e(t)\,e^2}$ is the wavelength of plasma wave and $n_e = (z_0 + ct - z_3)(n_0 - n_1)/L_{down} + n_1$ is electron density at the pulse center along density downramp, with $z_3 = z_1 + L_{up} + L_{flat}$ and $z_1 = 600.06$ mm. The magenta dotted, dashed and solid lines in Fig. 4(a) correspond to the cases of $n_1 = 2n_0$, $n_1 = 3n_0$, and $n_1 = 5n_0$, respectively. Figure 4(b) shows the change of the injected charge with the propagation distance. Figure 4(c) shows the energy spectrum of accelerated electrons at $t = 9.98$ ps (corresponding to the last column in Fig. 3). Figures 4(d)–4(f) show variations of the maximum on-axis electric field E_{max}, group velocity v_{fp} and focal spot size w_0 (defined by the first transverse zero position) with the propagation distance. Note that the simulated group velocity is defined as the velocity of the laser centroid, *i.e.*, $v_{fp} = \mathrm{d}z_c/\mathrm{d}t$.

Here $z_c = \int_0^{w_0}\int_{z_-}^{z_+} 2\pi rzI\mathrm{d}z\mathrm{d}r / \int_0^{w_0}\int_{z_-}^{z_+} 2\pi rI\mathrm{d}z\mathrm{d}r$ is the longitudinal centroid of laser pulse, and $z_\pm = z_0 + ct \pm l/2$, with l representing the pulse length, $I(z,r)$ being the laser intensity.

From Fig. 3(b), one can see that some electrons are initially injected at the tail of the bubble since the phase velocity of wakefield in density downramp is less than light speed c (see the solid red line in Fig. 4(a)). However, these electrons are quickly thrown out of the bubble during subsequent transverse oscillations (see Figs. 3(c) and 3(d)), resulting in no electrons being accelerated finally (see Fig. 3(e) and the red lines in Figs. 4(b) and 4(c)). This is different from the density transition injection in traditional LWFA, where a relatively small density gradient can inject and accelerate a large number of electrons.[26] There are two reasons for this phenomenon: (i) the group velocity of laser oscillates in low-density plateau and it may be superluminal, although its average value is equal to c, as shown in Fig. 4(e). The oscillations of group velocity mainly stem from its inherent interference effect (oscillation even in vacuum) and the influence of plasmas. (ii) A superluminal wakefield structure is different from a traditional subluminal one due to the different responses of electrons and the different evolution of laser pulses (a detailed study will be published in another paper), which leads to different focusing fields. Therefore, in order to eventually inject and accelerate more electrons, it is necessary to initially inject more electrons into the bubble and slightly away from the tail of the bubble. This means that a larger density n_1 in high-density plateau is required, which corresponds to a higher density gradient. As one can see from Figs. 3(g) and 3(l), more electrons are initially injected into the bubble due to a smaller (even negative) phase velocity of plasma wave (see green and blue solid lines in Fig. 4(a)). In this case, although some electrons are also lost during subsequent oscillations (see Figs. 3(h) and 3(i) and 3(m) and 3(n)) due to the superluminal group velocity (see green and blue lines in Fig. 4(e)) and pulse deformation, a considerable number of electrons are accelerated finally, as shown in Figs. 3(j) and 3(o). The green and blue lines in Figs. 4(b) and 4(c) indicate that a larger density n_1 allows more electrons to be injected and accelerated, but also reduces the energy of electron beam, which is similar to density transition injection in traditional LWFA.[26] Furthermore, as one can see from Figs. 4(d)–4(f), with the increase of n_1, the laser tends to propagate unstably, but this trend is weakened as the laser enters the low-density plateau.

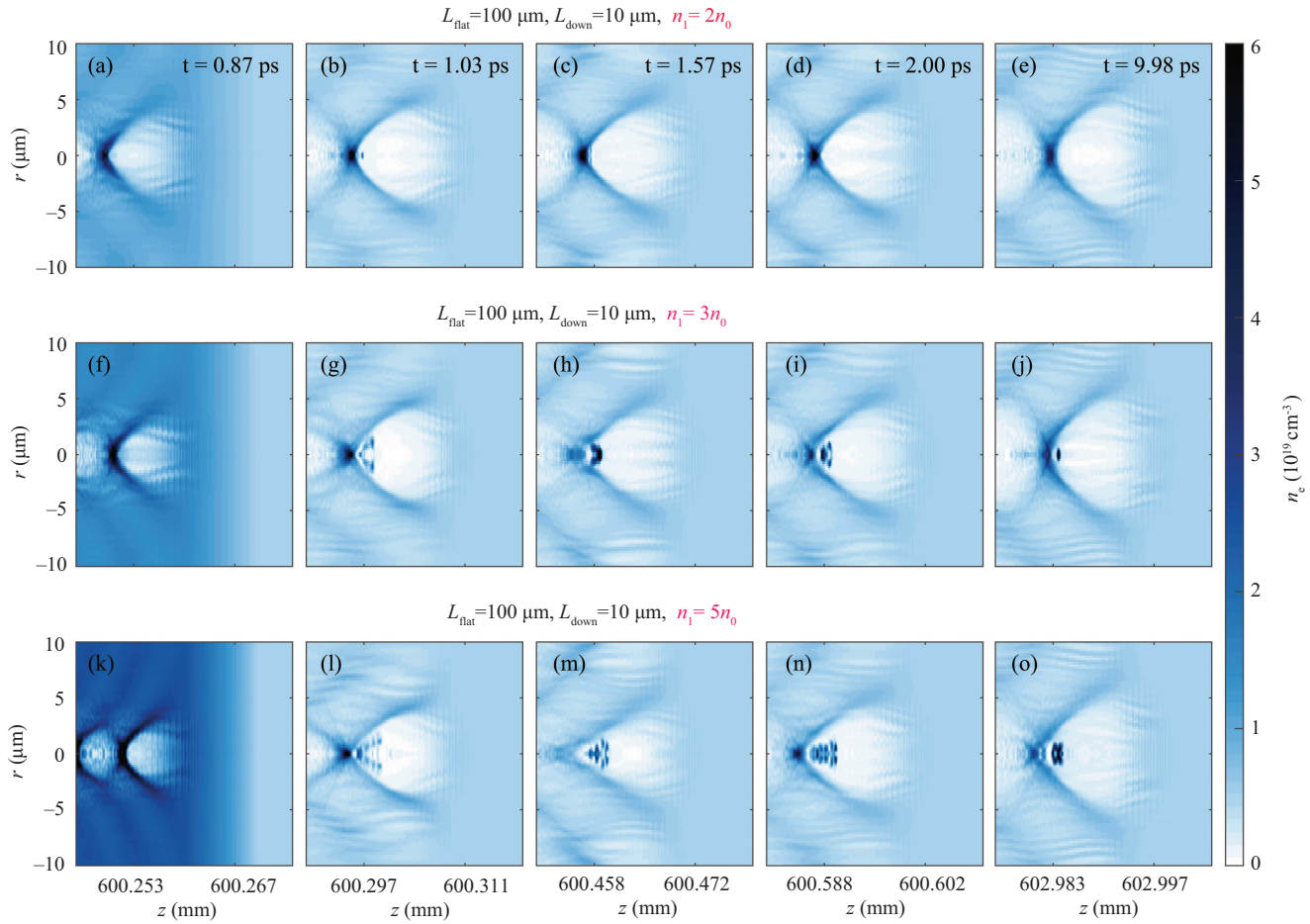


Fig. 3. Effect of high plateau density (n_1) on electron injection. The top panels (panels (a)–(e)) show spatial distribution of electron density at different instants when $n_1 = 2n_0$, while central and bottom panels correspond to $n_1 = 3n_0$ and $n_1 = 5n_0$, respectively. The first (panels (a), (f), (k)) and second (panels (b), (g), (l)) columns correspond to the moments before and after the laser enters the density downramp, respectively. The last column (panels (e), (j), (o)) corresponds to the moment when the laser propagates about 3 mm. Due to the electron loss caused by the possible superluminal group velocity and the change of wakefield structure, in phase-locked LWFA, in order to finally inject and accelerate more electrons, a larger n_1 is required.

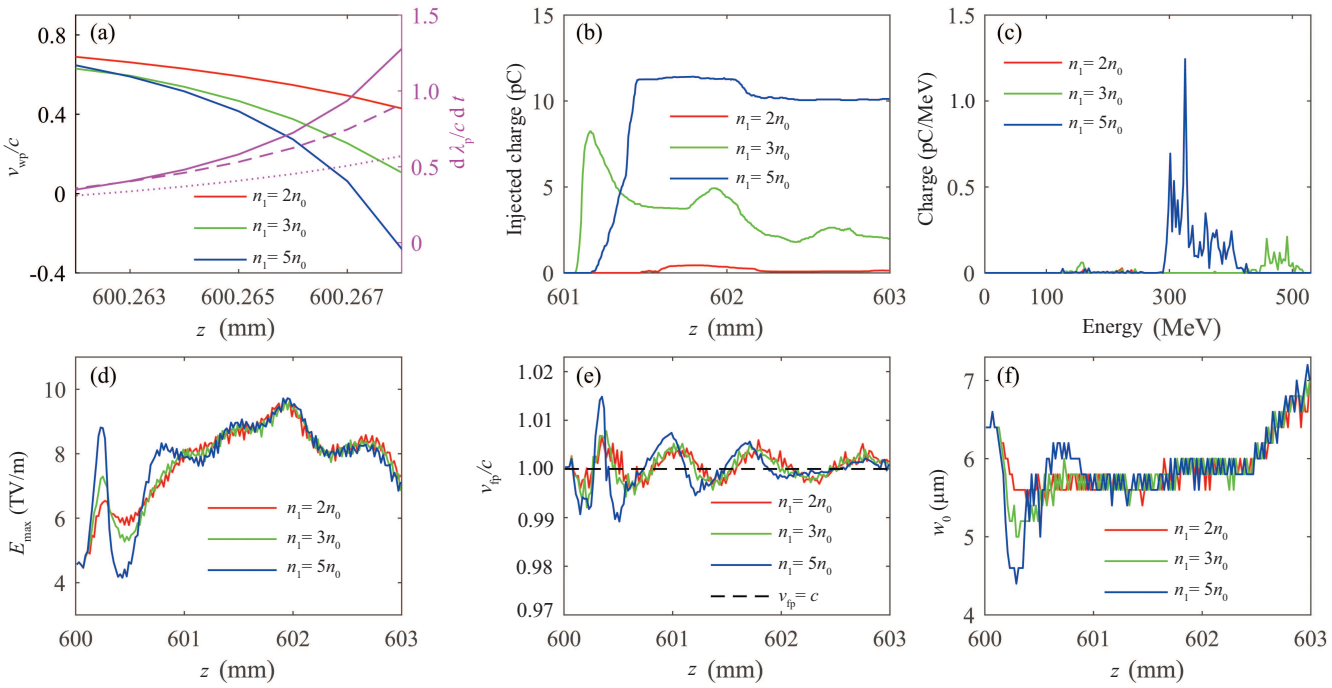


Fig. 4. Effect of high plateau density (n_1) on electron injection and laser propagation. (a) Phase velocity of wakefield v_{wp} (red, green, and blue lines) and expansion velocity of plasma wave $d\lambda_p/dt$ (magenta lines) along the density downramp. Magenta dotted, dashed, and solid lines represent $n_1 = 2n_0$, $n_1 = 3n_0$, and $n_1 = 5n_0$, respectively. (b) Injection charge varies with the propagation distance. (c) Energy spectrum of accelerated electrons at $t = 9.98$ ps, where the red, green and blue lines correspond to panels (e), (j), and (o) in Fig. 3, respectively. (d)–(f) Evolutions of the maximum on-axis electric field E_{max}, group velocity v_{fp}, and focal spot size w_0 of the laser with the propagation distance.

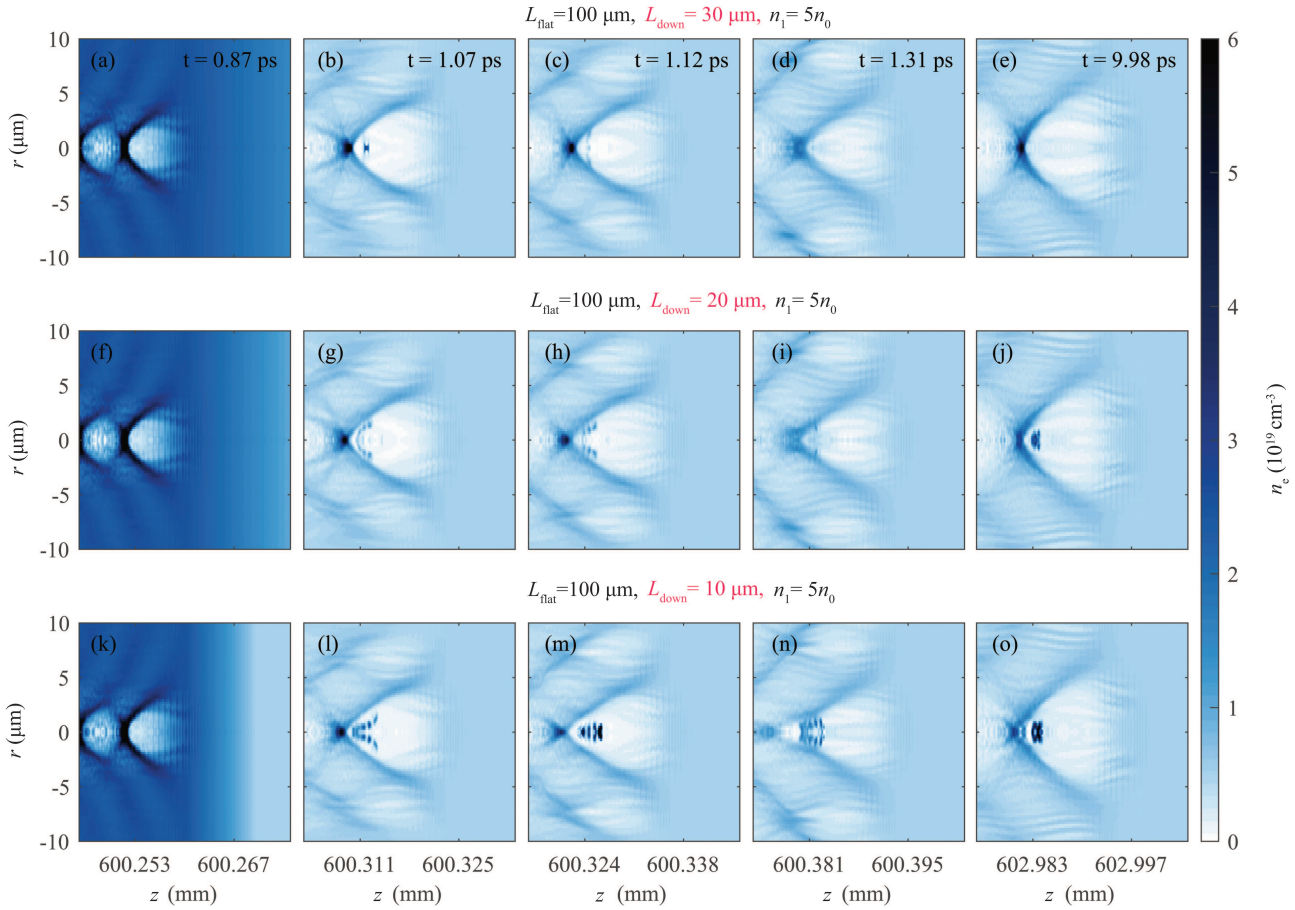


Fig. 5. Effect of density downramp length (L_{down}) on electron injection. The top panels (panels (a)–(e)) show spatial distribution of electron density at different instants when $L_{down} = 30$ μm, while central and bottom panels correspond to $L_{down} = 20$ μm, and $L_{down} = 10$ μm, respectively. The first (panels (a), (f), (k)) and second (panels (b), (g), (l)) columns correspond to the moments before and after the laser enters the density downramp, respectively. The last column (panels (e), (j), (o)) corresponds to the moment when the laser propagates about 3 mm. In phase-locked LWFA, in order to finally inject and accelerate more electrons, a shorter L_{down} is required.

3.2. Effect of density downramp length on injection

In addition to the high plateau density, the downramp length ($L_{\rm down}$) also affects the density gradient, thus affecting the electron injection. In order to study the effect of $L_{\rm down}$ on injection, a group of simulations are performed using parameters $L_{\rm flat} = 100$ μm, $n_1 = 5n_0$, and $L_{\rm down} = [30, 20, 10]$ μm. The simulation results are shown in Figs. 5 and 6. Figure 5 shows the spatial distribution of electron density at different instants. Figures 6(a)–6(c) are phase velocity of the wakefield (solid lines) and the expansion velocity of plasma wave (dashed lines) along the density downramp. The red, green, and blue lines correspond to $L_{\rm down} = 30$ μm, $L_{\rm down} = 20$ μm, and $L_{\rm down} = 10$ μm, respectively. Figure 6(d) is evolutions of the injected charge with the propagation distance. Figure 6(e) shows the energy spectrum of accelerated electrons at $t = 9.98$ ps (corresponding to the last column in Fig. 5). Figure 6(f) represents the change of laser group velocity with propagation distance.

As one can see from Fig. 5(b), for a longer downramp, when laser pulse passes through density downramp, some electrons are injected into the bubble due to the decrease of the wakefield phase velocity (see solid line in Fig. 6(a)). However, owing to the change of wakefield structure and the superluminal laser group velocity (see Fig. 6(f)), these electrons are quickly lost from the bubble in subsequent oscillations (see Figs. 5(c) and 5(d)), resulting in no electrons being accelerated finally (see Fig. 5(e) and red lines in Figs. 6(d) and 6(e)). This means that a shorter downramp $L_{\rm down}$ is required. As one can see from the central and bottom panels in Fig. 5, with the decrease of $L_{\rm down}$ (which corresponds to the increase of the density gradient), initially more electrons are injected into the bubble and away from the tail of the bubble (see Figs. 5(g) and 5(l)), which benefits from a smaller or even negative phase velocity of wakefield (see solid lines in Figs. 6(b) and 6(c)). Therefore, even though some electrons are lost in subsequent oscillations (see Figs. 5(h) and 5(i) and Figs. 5(m) and 5(n)), an enormous number of electrons are accelerated eventually (see Figs. 5(j) and 5(o)). The green and blue lines in Figs. 6(d) and 6(e) show that a shorter $L_{\rm down}$ benefits more injected electrons, but it also reduces the energy of electrons. This is because in the case with a smaller $L_{\rm down}$, more electrons are injected away from the tail of the bubble, where the acceleration field is reduced. Figure 6(f) indicates that the evolution of laser pulses is not sensitive to the parameter $L_{\rm down}$.

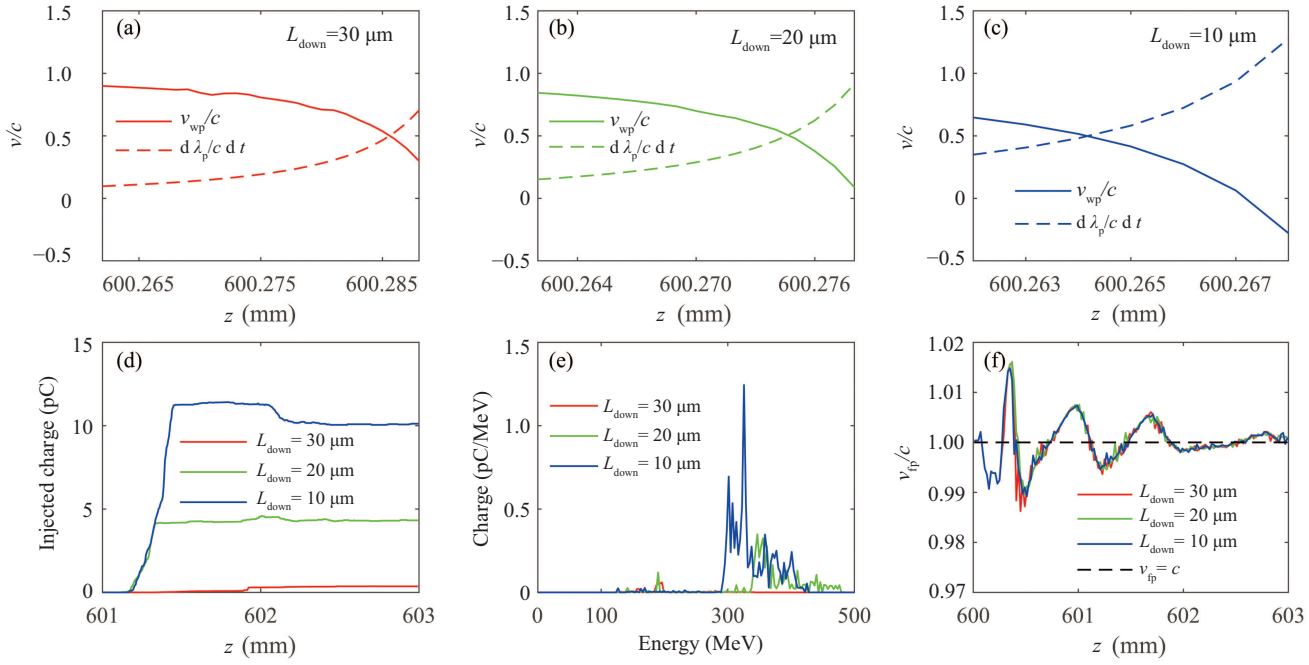


Fig. 6. Effect of density downramp length ($L_{\rm down}$) on electron injection and laser propagation. (a)–(c) Phase velocity of wakefield $v_{\rm wp}$ (solid lines) and expansion velocity of plasma wave d$\lambda_{\rm p}$/dt (dashed lines) along the density downramp for $L_{\rm down} = 30$ μm, $L_{\rm down} = 20$ μm, and $L_{\rm down} = 10$ μm. (d) The injected charge of electrons varies with the propagation distance. (e) Energy spectrum of accelerated electrons at $t = 9.98$ ps, where the red, green and blue lines correspond to panels (e), (j), and (o) in Fig. 5, respectively. (f) Evolution of laser group velocity with propagation distance.

3.3. Effect of high plateau length on injection

As discussed in Subsections 3.1 and 3.2, in phase-locked LWFA, a higher density n_1 and a shorter length $L_{\rm down}$, such as [$n_1 = 5n_0$, $L_{\rm down} = 10$ μm], are required to eventually accelerate a considerable number of electrons. However, different from the traditional Gaussian beam, when the high-intensity flying focus laser propagates in the high-density plasma, the focusing of the light from a larger radius is easily affected by the plasma density modulation, which leads to the deformation and fracture of laser pulses.[34] Therefore, the length $L_{\rm flat}$ of high-density plateau affects the laser propagation, and then affects the electron injection and acceleration. We perform a

set of simulations to reveal this phenomenon, with parameters $n_1 = 5n_0$, $L_{\rm down} = 10$ μm, and $L_{\rm flat} = [100, 300, 500]$ μm. The simulation results are shown in Figs. 7 and 8. Figure 7 shows spatial distribution of electron density at different instants. The first (Figs. 7(a), 7(f), 7(k)) and second (Figs. 7(b), 7(g), 7(l)) columns correspond to the moments before and after the laser enters the density downramp, respectively. The last column corresponds to the moment when the laser propagates about 3 mm. Figures 8(a)–8(c) show the spatial distribution of the laser transverse electric field $E_{\rm r}$ before entering density downramp. That is, figures 8(a)–8(c) correspond to the first column in Fig. 7. Figure 8(d) shows variations of the maximum on-axis electric field $E_{\rm max}$ with the propagation distance. The black circle, pentagram, and triangle correspond to the positions of Figs. 8(a)–8(c), respectively. The red, green, and blue lines represent the cases of $L_{\rm flat} = 100$ μm, $L_{\rm flat} = 300$ μm, and $L_{\rm flat} = 500$ μm, respectively. Figure 8(e) shows evolutions of the injected charge with the propagation distance. Figure 8(f) is the energy spectrum of the accelerated electrons at $t = 9.98$ ps.

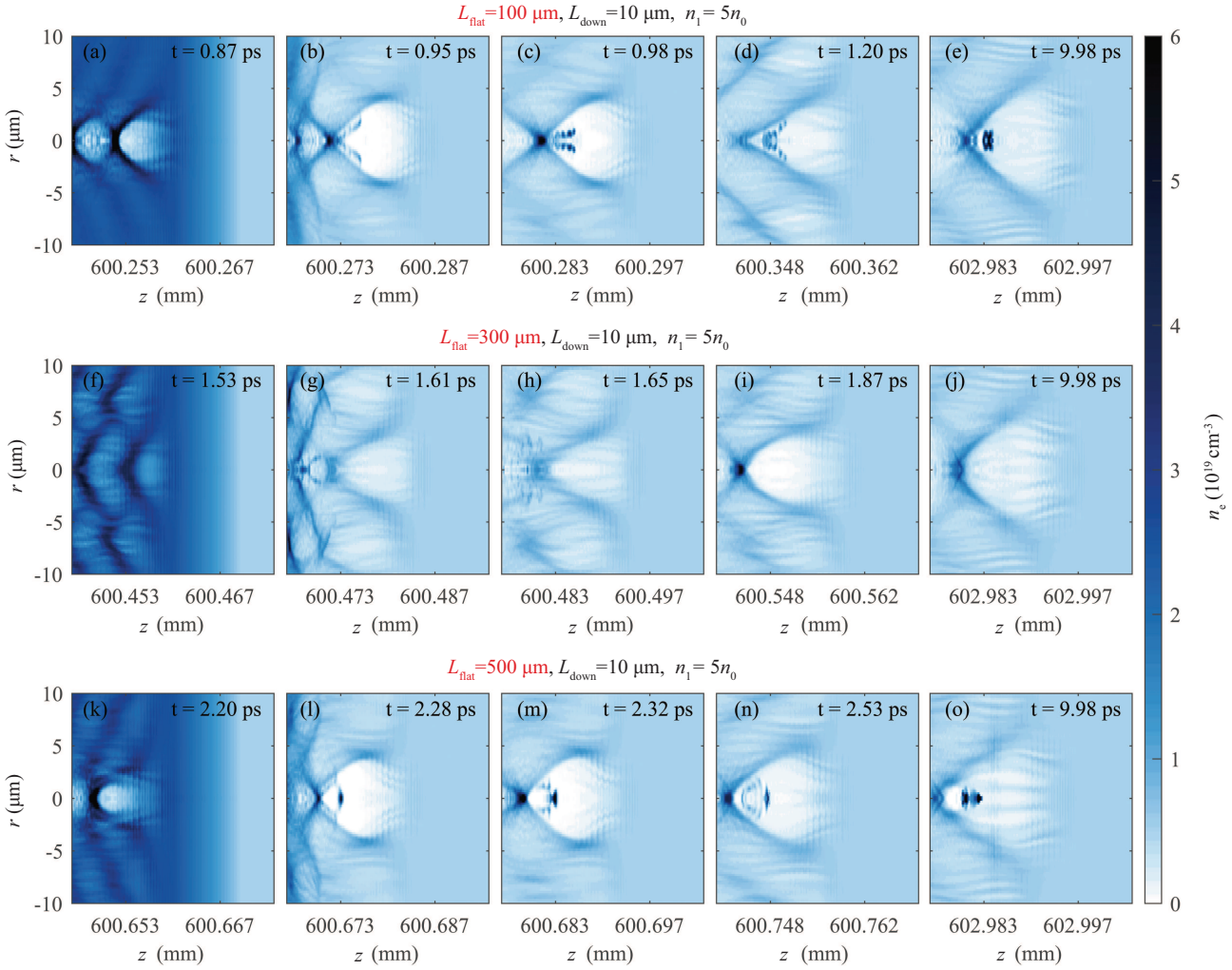


Fig. 7. Effect of high plateau length ($L_{\rm flat}$) on electron injection. The top panels (panels (a)–(e)) show spatial distribution of electron density at different instants when $L_{\rm flat} = 100$ μm, while central and bottom panels correspond to $L_{\rm flat} = 300$ μm, and $L_{\rm flat} = 500$ μm, respectively. The first (panels (a), (f), and (k)) and second (panels (b), (g), and (l)) columns correspond to the moments before and after the laser enters the density downramp, respectively. The last column (panels (e), (j), and (o)) corresponds to the moment when the laser propagates about 3 mm. Due to the unstable propagation of high-intensity flying focus lasers in high-density plasma, the electron injection also depends on the position of the density downramp.

As we can see from Fig. 7(a), when $L_{\rm flat} = 100$ μm, a strong wakefield is formed before entering density downramp, where the laser propagation is stable and its intensity is large (see Fig. 8(a) and black circle in Fig. 8(d)). Therefore, after a steep density downramp, a large number of electrons are injected and accelerated, as shown in Figs. 7(b)–7(e). However, as shown in the central panels of Fig. 7, when the length of high-density plateau increases to $L_{\rm flat} = 300$ μm, no electrons are injected and accelerated. This is because the propagation of laser is unstable before entering density downramp: the pulse appears obvious deformation and fracture, and thus its intensity is weak (see Fig. 8(b) and black pentagram in Fig. 8(d)). Therefore, the wakefield structure is destroyed and very weak before and after the laser enters density downramp, resulting in no electrons being captured and accelerated (see Figs. 7(f)–7(h)). When the length of high-density plateau

is further increased to $L_{\rm flat} = 500$ μm, the laser intensity increases again before entering density downramp (see Fig. 8(c) and black triangle in Fig. 8(d)). Therefore, the wakefield is enhanced again and a considerable number of electrons are injected and accelerated, as shown in Figs. 7(k)–7(m). However, it is important to note that the longer the laser travels in high-density plateau, the poorer the stability of the laser (see blue line in Fig. 8(d)). Therefore, in the case of a longer $L_{\rm flat}$, the stability and energy spectrum of accelerated electrons become worse, as shown by the blue line in Figs. 8(e) and 8(f). Figure 9 shows variation of injected charge with parameter $L_{\rm flat}$ at $t = 10$ ps. As one can see, no electrons are injected when $L_{\rm flat} \approx 300$ μm, while the obvious electron injection occurs at $L_{\rm flat} \approx 100$ μm and $L_{\rm flat} \approx 500$ μm, which is consistent with Figs. 7 and 8.

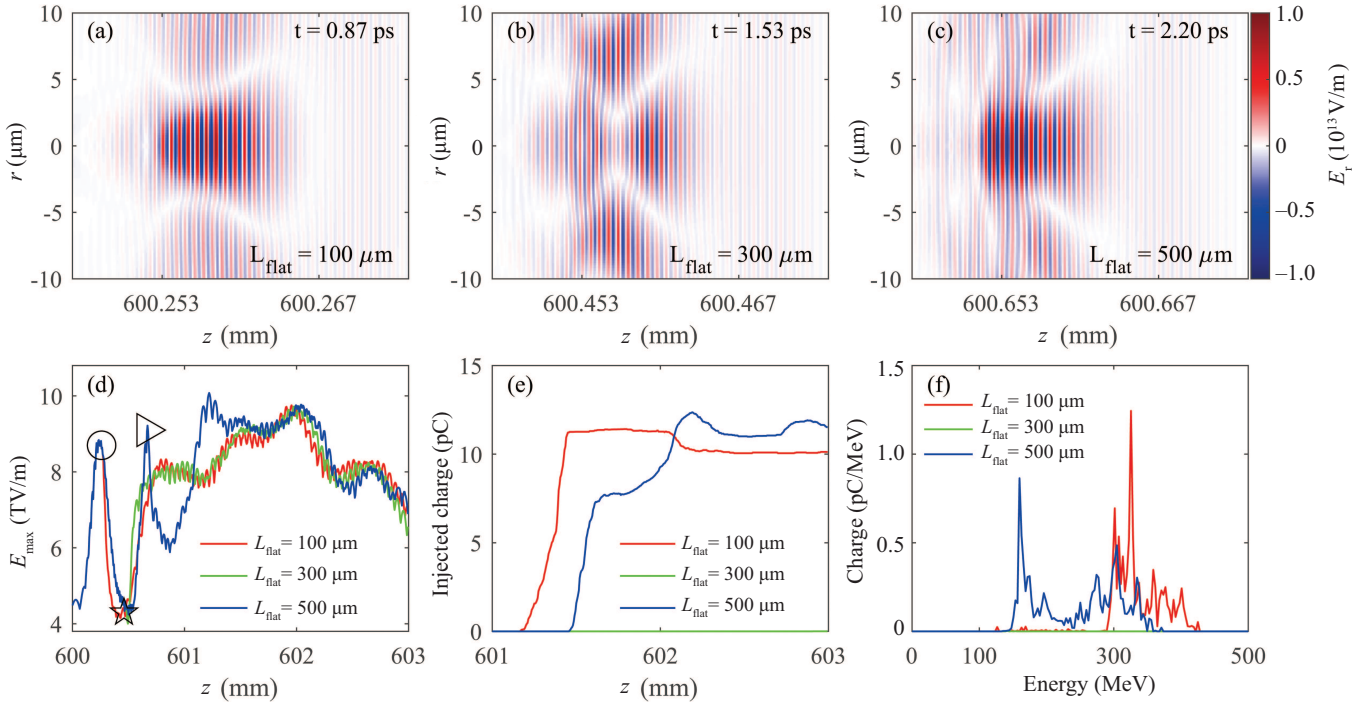


Fig. 8. Effect of high plateau length ($L_{\rm flat}$) on laser propagation and electron injection. (a)–(c) Spatial distribution of laser transverse electric field before entering the density downramp for $L_{\rm flat} = 100$ μm, $L_{\rm flat} = 300$ μm, and $L_{\rm flat} = 500$ μm, *i.e.*, corresponding to the first column of Fig. 7. (d) Evolution of the maximum on-axis electric field E_{max} with the propagation distance, where the black circle, pentagram, and triangle correspond to sub-figures (a)–(c). (e) The injected charge of electrons varies with the propagation distance. (f) Energy spectrum of accelerated electrons at $t = 9.98$ ps, where the red, green, and blue lines correspond to panels (e), (j), and (o) in Fig. 7, respectively.

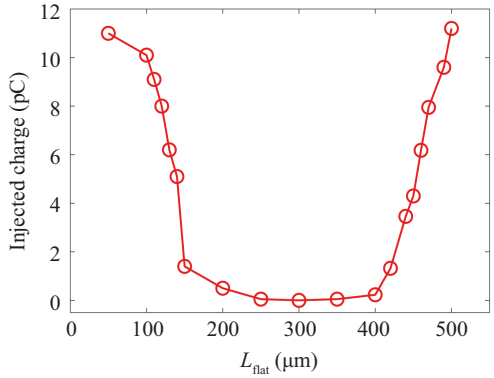


Fig. 9. Variation of injected charge with parameter $L_{\rm flat}$ at $t = 10$ ps. No electrons are injected when $L_{\rm flat} \approx 300$ μm. The obvious electron injection occurs at $L_{\rm flat} \approx 100$ μm, and $L_{\rm flat} \approx 500$ μm.

4. Conclusion

In summary, specific parameter effects on density transition injection of electrons in phase-locked LWFA are numerically studied by PIC simulations. We find that it is more difficult to inject electrons into the wakefield driven by a flying focus laser than by usual lasers. In order to inject and accelerate amount of electrons, a larger density gradient (*i.e.*, a shorter downramp and a higher density plateau) is required. When the density gradient is relatively small, although some electrons are initially injected into the bubble, these electrons are quickly thrown out of the bubble in subsequent oscillations, resulting in no electrons being accelerated. This is because the oscillating laser group velocity may be superluminal and the wakefield structure varies during the acceleration. Similar to density transition injection in traditional LWFA, a larger density gradient can inject more electrons in phase-locked LWFA, but also reduces their maximum energy. In addition, because the high-intensity flying focus laser will appear periodic deformation and fracture when propagating in the high-density plasma, the length of the high-density plateau $L_{\rm flat}$ can affect the laser propagation, thus affecting the electron injection. Along with the increase of $L_{\rm flat}$, the injection occurs periodically. However, a longer $L_{\rm flat}$ leads to an unstable laser propagation, which ultimately makes the acceleration stability and

energy spectrum worse. These results can provide guidance for future experiments of phase-locked LWFA.

Acknowledgments

Project supported by the National Natural Science Foundation of China (Grant Nos. 11991074, 12225505 and 12135009). The simulations were performed on the π 2.0 supercomputer in the Center for High Performance Computing at Shanghai Jiao Tong University.

References

[1] Tajima T and Dawson J M 1979 *Phys. Rev. Lett.* **43** 267
[2] Esarey E, Schroeder C B and Leemans W P 2009 *Rev. Mod. Phys.* **81** 1229
[3] Chen M, Liu F, Li B Y, Weng S M, Chen L M, Sheng Z M and Zhang J 2020 *High Power Laser Part. Beams* **32** 092001
[4] Li W T, Wang W T, Liu J S, Wang C, Zhang Z J, Qi R, Yu C H, Li R X and Xu Z Z 2015 *Chin. Phys. B* **24** 015205
[5] Zhang G B, Hafz N A M, Ma Y Y, Qian L J, Shao F Q and Sheng Z M 2016 *Chin. Phys. Lett.* **33** 095202
[6] Malka V, Fritzler S, Lefebvre E, Aleonard M M, Burgy F, Chambaret J P, Chemin J F, Krushelnick K, Malka G, Mangles S P D, Najmudin Z, Pittman M, Rousseau J P, Scheurer J N, Walton B and Dangor A E 2002 *Science* **298** 1596
[7] Leemans W P, Nagler B, Gonsalves A J, Toth C, Nakamura K, Geddes C G R, Esarey E, Schroeder C B and Hooker S M 2006 *Nat. Phys.* **2** 696
[8] Leemans W P, Gonsalves A J, Mao H S, Nakamura K, Benedetti C, Schroeder C B, Toth C, Daniels J, Mittelberger D E, Bulanov S S, Vay J L, Geddes C G R and Esarey E 2014 *Phys. Rev. Lett.* **113** 245002
[9] Gonsalves A J, Nakamura K, Daniels J, Benedetti C, Pieronek C, de Raadt T C H, Steinke S, Bin J H, Bulanov S S, van Tilborg J, Geddes C G R, Schroeder C B, Toth C, Esarey E, Swanson K, Fan-Chiang L, Bagdasarov G, Bobrova N, Gasilov V, Korn G, Sasorov P and Leemans W P 2019 *Phys. Rev. Lett.* **122** 084801
[10] Leemans W and Esarey E 2009 *Phys. Today* **62** 44
[11] Schroeder C B, Esarey E, Geddes C G R, Benedetti C and Leemans W P 2010 *Phys. Rev. ST Accel. Beams* **13** 101301
[12] Steinke S, van Tilborg J, Benedetti C, Geddes C G R, Schroeder C B, Daniels J, Swanson K K, Gonsalves A J, Nakamura K, Matlis N H, Shaw B H, Esarey E and Leemans W P 2016 *Nature* **530** 190
[13] Luo J, Chen M, Wu W Y, Weng S M, Sheng Z M, Schroeder C B, Jaroszynski D A, Esarey E, Leemans W P, Mori W B and Zhang J 2018 *Phys. Rev. Lett.* **120** 154801
[14] Guillaume E, Dopp A, Thaury C, Phuoc K T, Lifschitz A, Grittani G, God- det J P, Tafzi A, Chou S W, Veisz L and Malka V 2015 *Phys. Rev. Lett.* **115** 155002
[15] Zhu X Z, Chen M, Li B Y, Liu F, Ge X L, Sheng Z M and Zhang J 2022 *Phys. Plasmas* **29** 013101
[16] Zhu X Z, Li B Y, Liu F, Li J L, Bi Z W, Lu L, Yuan X H, Yan W C, Chen M, Chen L M, Sheng Z M and Zhang J 2022 *Acta Phys. Sin.* **71** 095202 (in Chinese)
[17] Marie A S, Gobert O and Quere F 2017 *Optica* **4** 1298
[18] Froula D H, Turnbull D, Davies A S, Kessler T J, Haberberger D, Palastro J P, Bahk S W, Begishev I A, Boni R, Bucht S, Katz J and Shaw J L 2018 *Nat. Photon.* **12** 262
[19] Debus A, Pausch R, Huebl A, Steiniger K, Widera R, Cowan T E, Schramm U and Bussmann M 2019 *Phys. Rev. X* **9** 031044
[20] Shalloo R J and Mangles S P D 2020 *Nat. Photon.* **14** 470
[21] Caizergues C, Smartsev S, Malka V and Thaury C 2020 *Nat. Photon.* **14** 475
[22] Palastro J P, Shaw J L, Franke P, Ramsey D, Simpson T T and Froula D H 2020 *Phys. Rev. Lett.* **124** 134802
[23] Smartsev S, Caizergues C, Oubrerie K, *et al*. 2019 *Opt. Lett.* **44** 3414
[24] Oubrerie K, Andriyash I A, Lahaye R, Smartsev S, Malka V and Thaury C 2022 *J. Opt.* **24** 045503
[25] Schmid K, Buck A, Sears C M S, Mikhailova J M, Tautz R, Herrmann D, Geissler M, Krausz F and Veisz L 2010 *Phys. Rev. ST Accel. Beams* **13** 091301
[26] Massimo F, Lifschitz A F, Thaury C and Malka V 2017 *Plasma Phys. Control. Fusion* **59** 085004
[27] Massimo F, Lifschitz A F, Thaury C and Malka V 2018 *Plasma Phys. Control. Fusion* **60** 034005
[28] Wang T and Wang X F 2016 *Acta Phys. Sin.* **65** 044102 (in Chinese)
[29] Chen M, Sheng Z M, Ma Y Y and Zhang J 2006 *J. Appl. Phys.* **99** 056109
[30] Pak A, Marsh K A, Martins S F, Lu W, Mori W B and Joshi C 2010 *Phys. Rev. Lett.* **104** 025003
[31] Cui Y, Zhang G B, Ma Y Y, Yang X H, Mu J Y, Yao H B, Zi M, Zhou J, Yang J Q, Hu L X and Tian L C 2021 *Chin. Phys. B* **30** 105201
[32] Buck A, Wenz J, Xu J, Khrennikov K, Schmid K, Heigoldt M, Mikhailova J M, Geissler M, Shen B, Krausz F, Karsch S and Veisz L 2013 *Phys. Rev. Lett.* **110** 185006
[33] Lehe R, Kirchen M, Andriyash I A, Godfrey B B and Vay J L 2016 *Comput. Phys. Commun.* **203** 66
[34] Geng P F, Chen M, Zhu X Z, Liu W Y, Sheng Z M and Zhang J 2022 *Phys. Plasmas* **29** 112301
[35] Oubrerie K, Leblanc A, Kononenko O, *et al*. 2022 *Light Sci. Appl.* **11** 180
[36] Fan Q P, Wen S L, Wang S Y, Yang Z H, Chen Y, Liu D X and Wei L 2021 *Phys. Scr.* **96** 065508
[37] Cui Z, Kang J, Guo A, Zhu H, et al. 2019 *Opt. Express* **27** 16812
[38] Sun B, Salter P S and Booth M J 2015 *Opt. Express* **23** 19348
[39] Fan Q P, Wang S Y, Wei L, Yang Z H, Zhang Q Q, Chen Y, Wu Y Z and Cao L F 2019 *Opt. Commun.* **453** 124342
[40] Sochacki J, Kotodziejczyk A, Jaroszewicz Z and Bara S 1992 *Appl. Opt.* **31** 5326